Elevated Momentum Flux in the Surfzone during a Storm

HENRY POTTER,[a] MENG LYU,[a] AND XIN YANG[b]

[a] *Department of Oceanography, Texas A&M University, College Station, Texas*
[b] *NOAA/AOML/Hurricane Research Division and University of Miami/CIMAS, Miami, Florida*

(Manuscript received 13 June 2024, in final form 3 March 2025, accepted 22 March 2025)

ABSTRACT: Drag coefficient parameterizations, which are largely developed from homogenous deep ocean data, are ineffective nearshore where conditions are nonuniform. This is problematic because operational forecast accuracy depends upon reliable quantification of air–sea momentum transfer. This is especially important for storms which threaten coastal life and property. To help fill this knowledge gap, direct flux measurements were collected from the beach and pierhead in Duck, North Carolina, as part of the During Nearshore Event Experiment (DUNEX). The footprint analysis shows these fluxes were sourced in the surfzone and offshore, representing very different conditions. During a weeklong storm, wind speeds and significant wave heights were 20 m s^{-1} and 4 m, leading to a broad, vigorous surfzone. The drag coefficient in the surfzone was twice the offshore value, explained by increased roughness due to wind stress and bathymetric changes. The Charnock parameter is well predicted by wave age, but it is expected this is site-specific due to unique bathymetry. A horizontal wind speed gradient was observed and attributed to the high surfzone roughness. The wavelengths of the turbulent eddies in the surfzone were smaller than offshore or predicted by universal scaling. This research offers novel insights that can contribute to a crucial collective effort to develop robust coastal flux models, leading to improved forecasting.

SIGNIFICANCE STATEMENT: When wind blows over the ocean, the energy associated with its motion is moved from the air into water. This energy transfer helps grow waves and drive currents which, via many pathways, alter the characteristics of the upper ocean and lower atmosphere. In turn, this affects weather and climate, so it is critical this energy exchange is accounted for in forecasts. Energy transfer is reasonably well understood in the deep ocean, but not nearshore where conditions are nonuniform and change quickly, especially in storms where very few measurements are made. To remedy this, data were collected in May 2022 during a storm in Duck, North Carolina, which had wind speeds of 20 m s^{-1} and 4-m wave heights. The extreme conditions created a very wide and energetic surfzone. Wind measurements were made on the beach and approximately 500 m offshore. Due to the rough surface, twice the energy was transferred from the air into the ocean in the surfzone than offshore and the wind speed decreased as it crossed the surfzone. Finally, the wavelengths of the wind that transfer energy into the ocean are much smaller than offshore or predicted by previous research.

KEYWORDS: Turbulence; Marine boundary layer; Severe storms; Air-sea interaction; In situ atmospheric observations

1. Introduction

Within the marine boundary layer, energy is exchanged across the air–sea interface through the vertical transport of horizontal momentum via the momentum flux $\boldsymbol{\tau}$. This exchange, which occurs constantly across 71% of Earth's surface, is integral to the climate system because it is responsible for wave growth (e.g., Lee and Monty 2020), wave breaking and their associated processes (e.g., Anguelova and Webster 2006), currents (e.g., Constantin 2021), ocean mixing and global circulation (McMonigal et al. 2023), and tropical cyclone (TC) intensity (e.g., Collins et al. 2018; Potter and Rudzin 2021). The momentum flux also alters the wind speed profile (e.g., Wu and Qiao 2022), making it an important consideration for offshore wind energy. Direct measurement of $\boldsymbol{\tau}$ requires sampling turbulent fluctuations of the horizontal downwind u and crosswind v velocity and correlating them with the vertical velocity w. In stationary and homogeneous conditions, $\boldsymbol{\tau}$ is assumed to be constant within the surface flux layer and above the viscous sublayer and is calculated from

$$\boldsymbol{\tau} = \rho[(-\overline{u'w'})\mathbf{i} + (-\overline{v'w'})\mathbf{j}]. \quad (1)$$

Here, $\mathbf{i}$ and $\mathbf{j}$ are the unit vectors along and perpendicular to the mean wind direction, overbars represent the time average $O(30)$ min, and primes denote the fluctuating components ($\overline{u'} = \overline{v'} = \overline{w'} = 0$). Most models use a bulk formula to determine the momentum flux:

$$|\tau| = \rho C_{D_z} U_z^2, \quad (2)$$

where C_D and U are the drag coefficient and mean wind speed, respectively, and subscript z is the measurement height above the surface. This is often converted to 10-m neutral-equivalent conditions (U_{10N}) using similarity theory (Monin and Obukhov 1954).

Decades of research have led to substantial improvements to C_D parameterization, but even the most robust models [e.g., Coupled Ocean–Atmosphere Response Experiment

Supplemental information related to this paper is available at the Journals Online website: https://doi.org/10.1175/JAS-D-24-0090.s1.

Corresponding author: Henry Potter, hpotter@tamu.edu

DOI: 10.1175/JAS-D-24-0090.1

(COARE); Edson et al. 2013] are developed from open-ocean measurements where conditions are spatially uniform. As such, they are often ineffective in the nearshore (e.g., Potter et al. 2022) because they do not account for nearshore variability where ocean transitions to land and surface gravity waves, which give the ocean its roughness, become controlled by bathymetry rather than wind. This widens the range of wave celerity and thus wave age when compared to open-ocean conditions. Furthermore, as waves approach shore, their shapes morph, and they become increasingly removed from their open-ocean forms. Over shoaling waves, C_D changes with the angle of the wind relative to the shoreline (Potter et al. 2022; Shabani et al. 2016). Smaller values during alongshore wind compared to onshore were attributed to the apparent wave steepness relative to the wind direction, with C_D during onshore wind twice expected open-ocean values. Ortiz-Suslow et al. (2018) also found C_D much higher on the inner shelf than expected for any given wind speed, which could not be accounted for by cross-shore distance. Furthermore, Mahrt et al. (1996) found C_D significantly larger for short fetch conditions, especially at high wind speeds. In contrast, Vickers and Mahrt (2010) showed that the aerodynamic roughness in the coastal zone during weak to moderate wind is smaller than that given by the COARE algorithm. The unique and complex regime of nearshore interaction of waves and currents further obscure the matter because the wind stress, which is generally assumed aligned with the wind, can veer from the mean wind direction (e.g., Potter et al. 2015a; Zhanget al. 2009; Ortiz-Suslow et al. 2015). This is more complicated in the presence of varying wind-swell incidence angles and wave energy which have been shown to alter C_D (Potter 2015).

Predicting C_D in the surfzone has its own unique challenges. Hansen and MacMahan (2019) determined surfzone foam increases the surface roughness and, therefore, also increases C_D, consistent with MacMahan (2017) who showed surfzone C_D is twice open-ocean values. Elevated surfzone C_D was also measured by Vugts and Cannemeijer (1981) and Smith and Banke (1975). However, breaking waves cause flow separation (Reul et al. 1999) which may reduce the momentum flux, and spray generated during breaking is believed to reduce the momentum flux by smoothing the surface (Makin 2005). Collectively, nearshore dynamics means it remains a significant challenge to accurately predict the impact of wind forcing and wind-driven processes along the coast. There is a critical need to identify the coastal processes that affect air–sea momentum transfer and quantify their impact so that robust models can be developed. To this end, we present results from fieldwork completed in 2023 at the Field Research Facility (FRF) in Duck, North Carolina (NC). Direct flux measurements during a storm show that the drag coefficient in the surfzone can be twice as high than outside of it.

2. The experiment

Data were collected at the U.S. Army Research and Development Center's FRF, Duck, North Carolina. FRF has a rich history of hosting ocean research campaigns including Coupled Air–Sea Processes and Electromagnetic Ducting Research (CASPER)-East (Wang et al. 2018), Sandy Duck (Reniers et al. 2004), and Cross-Shore Sediment Transport Experiment (CROSSTEX) (Maddux et al. 2007). Our research is part of the During Nearshore Event Experiment (DUNEX). DUNEX is a multiagency, academic, and nongovernmental organization collaborative experiment to study coastal processes during storms. The goal of DUNEX is to improve observational technologies and advance understanding and models for coastal storms (Cialone et al. 2023). FRF comprehensively monitors the coastal ocean including waves, tides, currents, sediment dynamics, and standard oceanic and atmospheric information. The seaward face at FRF is about 72° from the north and the shelf is wide with a gentle slope ($\sim$1 m km^{-1}) (Long and Oltman-Shay 1991). Typical wave periods at FRF are 8–10 s with waves beginning to be influenced by the bottom at depths 50–75 m and become shallow water waves at 5–8 m, approximately 500 m from the shoreline. A pier at FRF extends about 500 m offshore to the $\sim$6-m depth contour relative to mean water level (mwl) with an instrument tower at the pierhead. Approximately 30 m inland from the shoreline is a dune with maximum height $\sim$6 m above mwl (Brodie et al. 2019). Twenty meters further inland is the beach tower (aka Argus tower) which is principally used for optical remote sensing to make nearshore measurements (Holman and Stanley 2007).

For this experiment, a Campbell Scientific Infrared Gas Analyzer and Sonic Anemometer (IRGASON) was mounted 14.4 m above mwl at the pierhead. Two Gill R3-50 sonic anemometers were mounted on the beach tower, one at 14.4 m and one at 18.4 m. Waves used in this study were recorded by FRF using an array of pressure sensors mounted north of the pier at the 8-m isobath around 900 m offshore. This site is outside the surfzone and away from all irregular isobaths to minimize bathymetrically induced wave inhomogeneities. The instrument is hard-wired to shore, and data are analyzed hourly. Water level data come from a second array deployed at the 4.5-m isobath. We focus on two weeks in May 2022 when there was a strong frontal passage from the northeast which caused high wind speeds and waves. This led to a proliferation of wave breaking, whitecap production, and foam generation creating a surfzone that stretched far from shore. The storm also pushed the shoreline up the beach dozens of meters beyond its typical quiescent location and close to the beach tower. A map of the research site and photos from the Argus tower before and during the storms are shown in Fig. 1.

All anemometers recorded u, v, and w and air temperature at 20 Hz. The wind vectors were rotated so that u points into the mean wind direction and $\overline{v} = \overline{w} = 0$. Data were then broken into 30-min bins, and an established protocol for quality control was followed (e.g., French et al. 2007; Potter et al. 2015b). We set a threshold of $r^2 > 0.9$ for the cumulative summation of the flux to ensure atmospheric stationarity (Potter et al. 2022) and examined the Ogives (the cospectrum integrals) to ensure the averaging period captured all turbulent scales present (Fig. 2). Twenty-one percent of the data had to be discarded for not meeting the quality standards. Due to

FIG. 1. (top) FRF showing the pier and locations of the anemometers and wave array. The prevailing wind direction during the storm is shown. The image was generated using Google Earth. (bottom) FRF (left) during normal quiescent conditions on 5 May and (right) during the northeaster on 9 May. Both images were captured at 1400 local time. These photos were collected from the Argus Imagery Platform (Holman and Stanley 2007). For reference, the piles are approximately 12 m apart in the shorelinenormal direction.

flow distortion caused by the pier during offshore wind, and to ensure the wind traveled across the surfzone (rather than along the beach) before reaching the beach tower, we only use flux data for wind within ±75° from onshore. Both anemometers were new, and factory calibrated before deployment and agreed during a collocated postdeployment calibration.

3. Results

a. Water level

The mean water level during the storm was 0.65 m above normal and had an approximate range of 0.6 m, shown in Fig. 3. The elevated water level started abruptly on 8 May and ended around 13 May, coinciding with the storm. The average foreshore slope at FRF is 1:12 (Plant and Holman 1997; Brodie et al. 2019), so the mean water level was 8.1 m further onshore than normal. The shoreline location was further impacted by wave run-up which can be estimated following Stockdon et al. (2006). This formula is used to determine the height that the 2% highest waves will reach on a beach (i.e., the discrete water-level maxima).

$$R_{2\%} = 1.1\left\{\frac{0.35\tan\beta(H_s L_0)^{1/2} + [H_s L_0(0.563\tan\beta^2 + 0.004)]^{1/2}}{2}\right\}, \quad (3)$$

where H_S is the significant wave height, L_0 is the average wavelength, and β is the beach slope. During the peak of the storm, significant wave height reached 4.1 m and wavelength L_0 was 131.7 m. Given the average foreshore slope of 0.08, the resulting run-up height $R_{2\%}$ = 15.5 m. This means the highest 2% of waves traveled 15.5 m up the beach from the mean water level. Therefore, the combined elevated water level and run-up pushed the water up the beach to the base of the dune, approximately 26 m from the tower. This is reflected in Fig. 1. This impacted the water-relative heights of the anemometers on the beach tower and has implications for the flux footprint (see section 4a).

b. Time series

Wind speeds and drag coefficients recorded at the pier and beach towers and waves recorded by the array are shown in Fig. 4. The northeaster is identifiable on 8 May by the rapid increase in wind speed and wave height and ended on 13 May

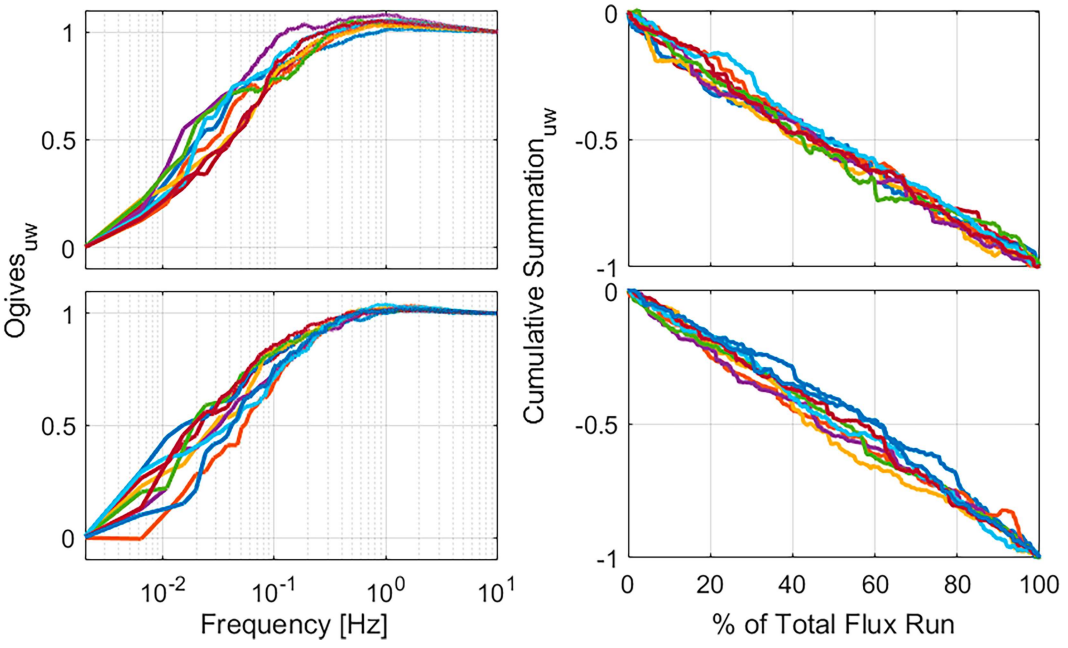

FIG. 2. (left) Ogives and (right) cumulative summations of the flux recorded simultaneously (top) at the pierhead and (bottom) on the beach at 18.4 m for the downwind covariance. In every subplot, the seven lines each come from 30 min of data collected on 9 May around the peak of the storm. Results were similar for data collected before and after the storm and for the flux recorded at 14.4 m but are not shown here.

when prestorm conditions returned. Mean wind direction was 9° from north (Fig. 1). At its peak, significant wave height was 4 m and wind speeds were 19.5, 18. 5, and 16 m s^{-1} for the pier and the 18.4- and 14.4-m beach towers, respectively. Drag coefficient data, only plotted for wind ±75° from onshore, agree at low winds and wave heights (~5–10 m s^{-1} and ~0.5 m) around 5–7 and 18–19 May, but diverge during the storm. Pier tower drag coefficient (C_{Dz_P}) was of typical order and follows a trend that mimics the wind speed. The beach tower drag coefficient at 18.4 m ($C_{Dz\_B18.4}$) also follows a wind speed trend but at higher values than C_{Dz_P}. Beach tower drag coefficient at 14.4 m ($C_{Dz\_B14.4}$) was much higher than both, and wind speed dependence, if any, is less clear.

c. *Directional dependence*

Drag coefficient as a function of wind direction is plotted in Fig. 5. This figure incorporates all data collected during this experiment's continuous measurement period 22 April–12 July. This image is very similar to Fig. 6 of Grachev et al. (2018) who recorded fluxes at the same location. They showed that for wind around 9° (north) (as was the case during our storm), the drag coefficients recorded at 10.1 and 14.4 m above mwl were characteristics of inland footprints while those at 22.5 and 31 m above mwl were characteristic of oceanic footprints. Our figure agrees, showing that $C_{Dz\_B14.4}$ has a peak for $25 > ^{\circ}$ (north) > 350 independent of wind speed, characteristic of an inland footprint. For $C_{Dz\_B18.4}$, there is no

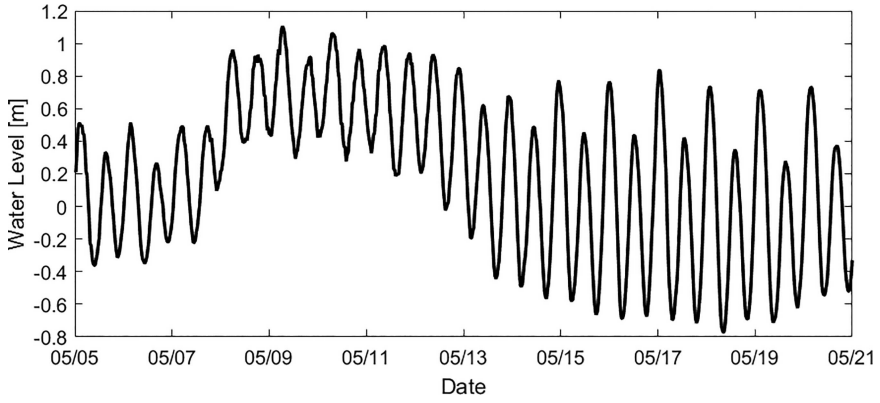

FIG. 3. Water level at the FRF.

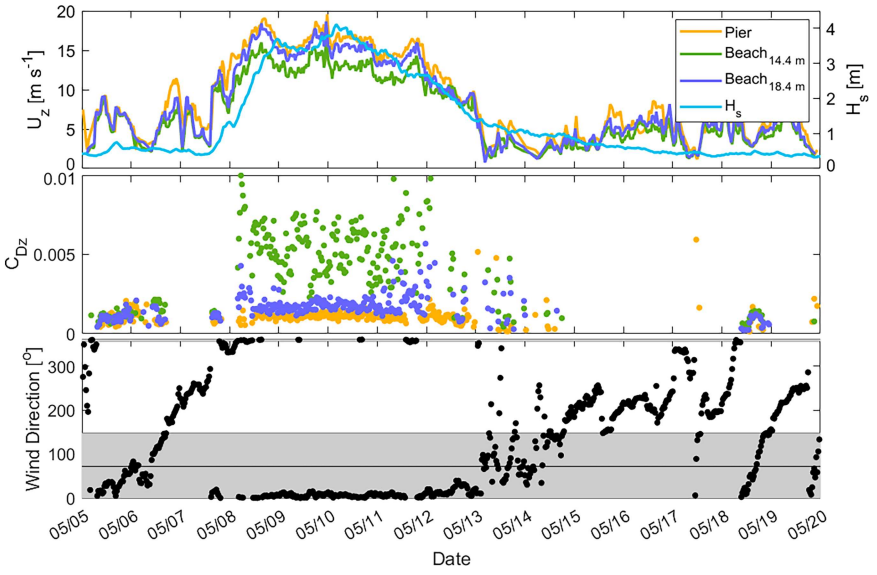

FIG. 4. (top) Wind speeds and significant wave height, (center) drag coefficient, and (bottom) wind direction. Drag coefficients are only plotted during periods of onshore wind (±75°). The wind direction displayed was measured at 18.4 m and gray shading show when wind was (±75°).

such peak in this directional range, save the nominal increase associated with high wind speed, meaning 18.4-m data are characteristics of an oceanic footprint. Hence, the transition from terrestrial to oceanic footprint at this location for northerly winds occurs between 14.4 and 18.4 m. This transition can be viewed in terms of the internal boundary layer (IBL). The IBL is formed when air flows over the ocean and onto land and begins to adjust to the new, rougher surface. An IBL is formed close to the ground that is adjusting to the new conditions and is characterized by the influence of the beach (rather than the ocean). The IBL will continue to grow vertically as the air moves downwind. For alongshore winds, the anemometer at 14.4 m is within the IBL but the anemometer at 18.4 m is outside the IBL. Figure 5 shows that C_D at both heights generally agree, except during alongside wind. This is because under these conditions, the spatial scale of interaction between the wind and beach is much longer than during onshore wind, so the IBL has greater opportunity to grow before reaching the flux tower. The intent of this paper is to quantify the spatial variability of the oceanic momentum flux during a storm. Since the data at 14.4 m during the storm capture the terrestrial flux, not the ocean flux, they will not be considered further in this analysis.

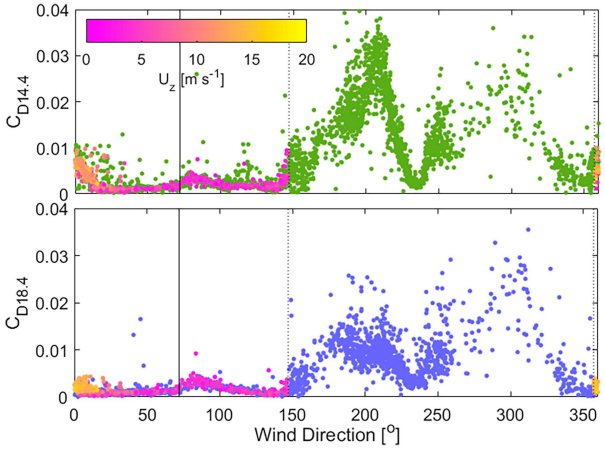

FIG. 5. The drag coefficient measured from the beach tower at (top) 14.4 m (green dots) and (bottom) 18.4 m (purple dots) as a function of wind direction. The black vertical line at 72° is directly onshore and the dashed vertical lines are ±75°. The data used in this manuscript collected between 5 and 20 May, as with Fig. 4, are shown by colored dots that indicate wind speed.

4. Discussion

a. *Flux footprint*

Two anemometers recorded the air–sea momentum flux during a storm. One was mounted 18.4 m on the beach tower and the other was mounted at 14.4 m at the pierhead. We now need to consider the upwind distance x over which the fluxes originated. These flux footprints assume skewed probability density functions $f(x, z)$ with peak at x_f and are often estimated using flux models. Here, we utilize footprint prediction from Kljun et al. (2015) for which the authors kindly provide the source code (footprint.kljun.net/index.php). This model was developed and evaluated using simulations of the backward Lagrangian stochastic particle dispersion model (Kljun et al. 2002) which tracks particles back in time from the receptor location to the surface source. Lagrangian stochastic models are one of the most accurate approaches to represent the flow around eddy-covariance towers, especially when there are obstacles or sharp changes in surface heterogeneity (Rey-Sanchez et al. 2022).

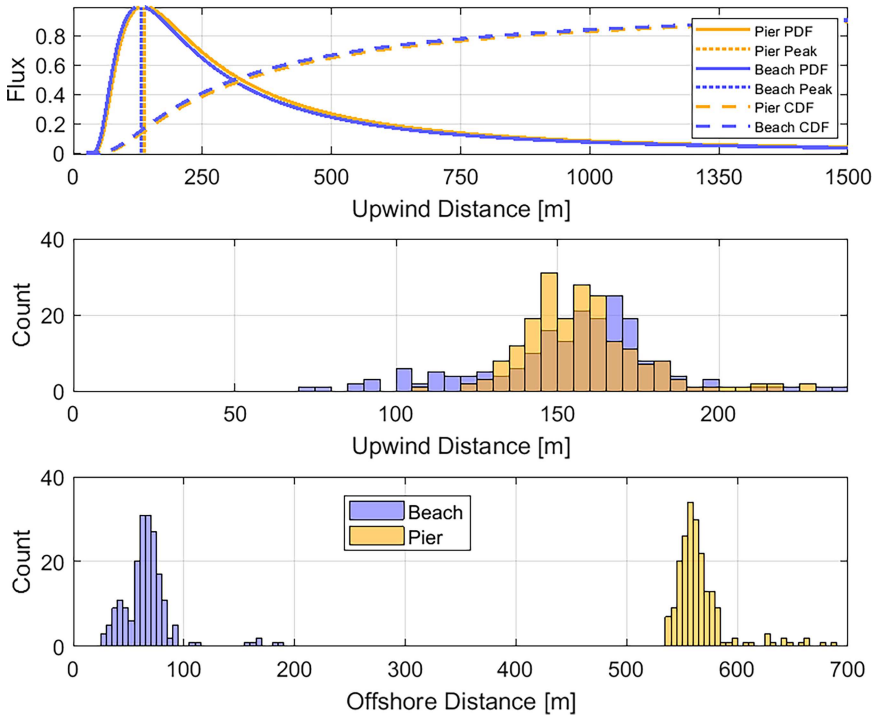

FIG. 6. (top) Probability density and cumulative density functions of mean flux footprints for the beach and pierhead anemometers 8–13 May. The y axis has been standardized to 1. (middle) Flux footprint peak upwind source location, $x_{f_{\text{beach}}}$ and $x_{f_{\text{pier}}}$ every 30 min. (bottom) Flux footprint peak offshore source location.

We executed the model using z, U_z, Obukhov length, friction velocity, roughness length, and boundary layer height. The Obukhov length (Obukhov 1946) is a ratio of shear to buoyant production of turbulence,

$$L = -\frac{u_*^3 \overline{\theta_v}}{\kappa g(\overline{w'\theta_v'})}. \tag{4}$$

Here, $g = 9.8\ \text{m s}^{-2}$ is the acceleration due to gravity, $\overline{\theta_v}$ is the mean virtual temperature, $\overline{w'\theta_v'}$ is the virtual temperature flux, and k is the Von Kármán constant = 0.41. The friction velocity comes from

$$u_* = \left|\frac{\boldsymbol{\tau}}{\rho}\right|^{1/2}, \tag{5}$$

and the roughness length, a measure of terrain roughness, is

$$z_0 = \frac{z}{e^{(U_z k/u_*)}}. \tag{6}$$

All variables were derived from anemometer data except boundary layer height which we set to 750 m because it is a good approximation (Lavers et al. 2019). Altering this value within reasonable bounds made little difference to the model output. We ran the model using mean values for the pier and beach towers collected during the northeaster (8–13 May, ~200 runs) to estimate x_f, flux footprint, and cumulative distributions of the flux. Please see Fig. 6.

The footprints for fluxes captured on the beach and pier are alike. Average $x_{f_{\text{beach}}} = 131\,\text{m}$ and average $x_{f_{\text{pier}}} = 138\,\text{m}$ (Fig. 6, top). Fifty percent of the flux was sourced within 308 m for the beach tower and 356 m for the pierhead, while 75% was sourced within 676 m from the beach and 715 m from the pierhead (Fig. 6, middle). This means the footprints shift continuously but their general forms remain. The bottom panel of Fig. 6 shows the offshore flux distance. This was calculated using the peak flux distance and the wind direction (i.e., $x_f[\cos°]$), then accounting for the distance from the anemometer to the mean waterline. This resulted in mean offshore distance to peak flux of 80 m for the beach anemometer and 560 m for the pierhead anemometer.

There is inherent uncertainty associated with estimating the flux footprint in the coastal zone. The Kljun et al. (2015) model assumes conditions adhere to Monin–Obukhov similarity theory and accounts for the Obukhov length when estimating the footprint. This is one of many models that use this approach or some other stability correction. Issues arise because Monin–Obukhov similarity theory assumes horizontal homogeneity of the surface, which is violated near shore. The problem is compounded because, even over the open ocean, momentum flux gradients are only constant 30%–40% of the time (Ortiz-Suslow et al. 2021). Because footprint models are developed for terrestrial environments, they do not account for the constantly shifting roughness of the ocean nor the nearshore where the surface morphs over short distances. Broadly,

nonconfirmation to similarity theory is a challenge to be overcome in marine boundary layer research. Specifically, this means errorless estimates of flux footprints are unavailable here, and when we employ the Kljun et al. (2015) model, we do so recognizing its limitation. Nonetheless, results indicate that the source location of the fluxes recorded on the beach was the surfzone, and the source location of the fluxes recorded at the pierhead was well beyond the surfzone. Hence, C_{Dz} at each of these locations represent very different regimes.

b. The drag coefficient

Figure 7 shows C_{Dz} as a function U_z. Data from Potter et al. (2022) which were collected from the FRF pierhead from August 2021 to February 2022 are also shown. Here, and throughout the study, we use measured values rather than their 10-m neutral equivalents. This is to avoid errors associated with the conversion when conditions do not adhere to the assumption of similarity theory, as is the case nearshore. Nonetheless, we found that during the storm, the mean atmospheric stability $z/L = -0.544$, which is in the range of neutral conditions, $-0.1 < z/L < 0.05$ (e.g., Smith 1980). At lower wind speeds, conditions were not neutral. Figure S1 in the online supplemental material shows stability as a function of wind speed for the data included in Fig. 7. Also plotted in Fig. S1 is C_{D10N} as a function of U_{10N}. This illustrates that converting to 10-m neutral-equivalent values has little impact on the results. We cautiously provide this figure as a supplement to allow our results to be compared to others which use the U_{10N} standard. Across the wind speed range, C_{Dz_P} during the northeaster agrees with these reference data, but $C_{Dz\_B18.4}$ agrees only up to ~11 m s^{-1} beyond which they diverge and $C_{Dz\_B18.4}$ is higher. Over the range of 11–20 m s^{-1}, mean $C_{Dz\_B18.4}$ is approximately double C_{Dz_P}. Our values for $C_{Dz\_B18.4}$ are aligned with those previously reported for the swash zone (Vugts and Cannemeijer 1981), surfzone (MacMahan 2017; Shabani et al. 2014), over shoaling waves (Shabani et al. 2016), and across the inner shelf (Ortiz-Suslow et al. 2018). Collectively, these report $C_D \sim$ 2–4 times greater than the open ocean. Among these, perhaps, the most comparable to our study is Shabani et al. (2014) who collected fluxes over the surfzone using two anemometers. They found the drag coefficient changes with the wind angle of approach relative to the shoreline and that C_D is much smaller for alongshore than onshore wind. This wind-wave angle relationship has been shown elsewhere (e.g., Ardhuin et al. 2007; Shabani et al. 2016; Potter et al. 2022). Their highest drag coefficients for onshore wind were about twice the values typical of the open ocean at similar wind speeds. However, for alongshore wind, C_D was approximately equal to those in the open ocean at comparable wind speed $O(10^{-3})$. They attributed this to apparent wave steepness (i.e., the increase in distance between wave crests as winds-wave angle increases). On the inner shelf, Ortiz-Suslow et al. (2018) also found wind-wave alignment led to a doubling of C_D. Our data are an interesting counterpart to these because they show that $C_{Dz\_B18.4}$ is double the offshore values for alongshore winds (recall Fig. 4). In other words, $C_{Dz\_B18.4}$ was twice

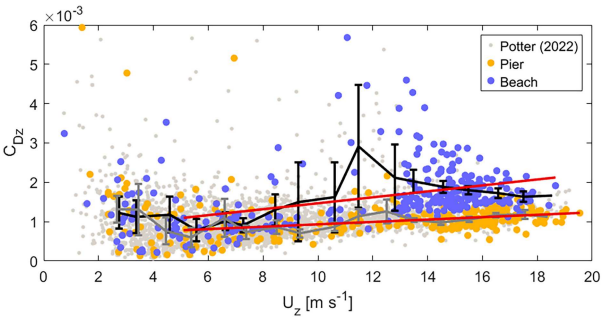

FIG. 7. Drag coefficient as a function of wind speed. The gray dots are from Potter et al. (2022) collected at the pierhead. The black and gray lines are mean and 95% confidence intervals for $C_{Dz\_B18.4}$ and C_{Dz_P}, respectively, and the burgundy lines are the linear fits from 5 m s^{-1}.

C_{Dz_P} *despite* winds being approximately perpendicular to the waves. Conceivably, $C_{Dz\_B18.4}$ would have been larger still if the wind was aligned with the waves and the apparent wave steepness was higher.

Regressions for $C_{Dz\_B18.4}$ and C_{Dz_P} for wind speeds 5–19 m s^{-1} are plotted in Fig. 7. Studies have shown that over this wind range, the relationship is generally linear (e.g., Edson et al. 2013; Potter et al. 2015b). The slopes are 7.56×10^{-5} and 3.03×10^{-5} for $C_{Dz\_B18.4}$ and C_{Dz_P}. These are significantly different from zero and from each other ($p \ll 0.01$). The difference in slopes shows the drag coefficient inside the surfzone grew over twice the rate as outside as winds strengthened. During the storm, H_s surged to 4 m in just over 24 h. Adopting a breaker index of 0.78 and the beach slope from Brodie et al. (2019), we can estimate the growth of the surfzone through breaking depth and location. For H_s of 1, 2, 3, and 4 m, breaking depths are ~1.3, 2.5, 3.8, and 5.2 m, respectively, amounting to approximate offshore distances of 50, 150, 250, and 450 m. Once at its peak, the storm lasted 2.5 days while the surfzone extended about half a kilometer from shore. Hence, the intensifying storm created waves which grew in height and spatial coverage. This increased the surfzone area within the flux footprint while increasing the roughness of the surfzone itself, raising the drag coefficient.

c. Nondimensional roughness

During the northeaster, the shallow water wave celerity $c_p = \sqrt{gh}$ shoreward of the pierhead was approximately 2–8 m s^{-1}, meaning the wind was outpacing the waves. In deep and intermediate depth water, the surface roughness is wave age dependent, commonly determined using

$$gz_0/u_*^2 = A\left(c_p/u_*\right)^{-B}. \tag{7}$$

The left side of this equation is the Charnock coefficient α used to quantify normalized roughness, and on the right side, c_p/u_* is the wave age. The Charnock coefficient decreases with wave age, meaning growing seas have higher Charnock

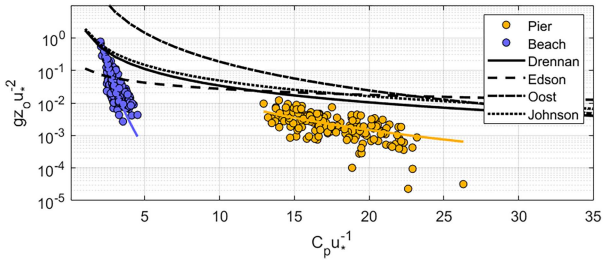

FIG. 8. Charnock coefficient as a function of wave age for $U_z > 13$ m s^{-1}. Pier and beach data are fitted with lines using $Y = aX^{-b}$. Lines from Drennan et al. (2003), Edson et al. (2013), Oost et al. (2002), and Johnson et al. (1998), using the same equation form, are also shown.

coefficients than developed seas, which have higher coefficients than decaying seas. Typical wave ages are 10–20 for growing seas, 20–30 for fully developed seas, and 30–40 for decaying seas. The Charnock coefficient is plotted as a function of wave age in Fig. 8. To ensure substantial surfzone area within the flux footprint and because of our interest in storm conditions, only data collected above 13 m s^{-1} ($H_s \gtrsim 3$ m) were used, resulting in ~175 data points (3.5 days) for each anemometer. For the pierhead, we used C_p from the array at the 8-m isobath, the closest direct measurement. For the surfzone, we used the shallow water wave approximation for C_p using the depth at the mean of the offshore distance to peak flux footprints. For comparison, curves from Drennan et al. (2003), Edson et al. (2013), Oost et al. (2002), and Johnson et al. (1998), developed from Eq. (7), are also shown. For our curves, the best fits are $gz_0/u_*^2 = 12.2(c_p/u_*)^{-3}$ and $gz_0/u_*^2 = 273.9(c_p/u_*)^{-8.4}$ for shoaling waves (pierhead) and surfzone (beach), with $r^2 = 0.35$ and $r^2 = 0.87$, respectively.

In the deep ocean, the Charnock parameter quantifies how winds stress influences the roughness of the sea surface because it is only through momentum exchange that roughness grows. However, near the shore, the Charnock parameter reflects roughness due to bathymetry and as well as wind stress. Furthermore, the wave age is controlled by bathymetrically induced changes to the wave phase speed such that the wind outpaces the waves ($C_p/U_z \ll 1$), which themselves are morphed through bathymetric changes. This makes direct α comparison between coastal and deeper water conditions somewhat impractical. Nevertheless, results in Fig. 8 show that at both locations, the Charnock parameter was lower than previous studies for comparable wave ages. This may be attributed in part to the reduction in the friction velocity for wind-wave misalignment identified by Manzella et al. (2024), Potter et al. (2022), and Shabani et al. (2014). This reduces the drag coefficient up to 50% inside and outside the surfzone, with greater impact at higher wind speeds (Potter et al. 2022). We suppose that because the wind was perpendicular to the waves, the momentum exchange did not translate to increased roughness as readily as it would have if the wind and waves were aligned. Shabani et al. (2014) found mean $\alpha = 0.1$, approximately double our surfzone mean, $\alpha = 0.058$, but because these data distribute logarithmically, the median $\alpha = 0.02$ is probably a more informative measure. Drag coefficient parity exists between these two studies, but higher wind speeds observed here translate to higher friction velocity. It is therefore noteworthy that the nondimensional roughness is greater for Shabani et al. (2014). This too may, in part, be because momentum exchange during alongshore winds does not translate so readily to increasing roughness. During the storm, the Iribarren parameter, which quantifies the ratio of seabed slope to wave steepness (Battjes 1974), was ≈0.1. This means the waves were spilling breakers characterized by gradual breaking over large distances with defined whitecaps at the crest and extensive wake foam. Surfzone foam has elevated z_0 which increases C_D independent of wind speed by about 50% (Hansen and MacMahan 2019) and, to some extent, helps explain elevated $C_{D\_B18.4}$. Also important is the shape of the breaking waves themselves which assume something akin to a sawtooth, creating more extreme roughness elements for which the wind to interact.

d. Wind speed reduction

During the storm, the wind speed recorded upon the beach at 18.4 m, $U_{z\_B18.4}$, was ~5% slower than that recorded at the pierhead U_{z_P}, which was not the case during more benign conditions. Furthermore, the beach anemometer was 4 m higher than the pierhead anemometer, so would typically be expected to record higher winds speed. Assuming a standard log profile, we used the wind speed at 18.4 m to estimate the wind at 14.4 m, allowing for a like-for-like comparison between the beach and pierhead. Doing so showed that the wind speed decreased 9% across the surfzone. Moreover, we can compare U_{z_P} to the actual wind speed recorded at 14.4 m, $U_{z\_B14.4}$ (recall Fig. 4), for which a decrease of 18% occurred over the same distance. According to Monin–Obukhov similarity theory (Monin and Obukhov 1954), the friction velocity should have a reciprocal relationship with wind speed. This has been experimentally proven many times (e.g., Yelland and Taylor 1996; Sahlée et al. 2012) but is not true for these moderate–high wind speed nearshore data where pierhead wind speed is higher but fluxes are lower. This suggests that elevated drag in the surfzone gave rise to the horizontal wind speed gradient. In other words, the high surface roughness in the surfzone appears to have dragged the wind, slowing it as it approached the beach. This effect was amplified for $U_{z\_B14.4}$ because of interaction with the beach itself. Decreases in terrestrial wind speed due to increased surface roughness through land use change are well reported (e.g., Pryor et al. 2009; Guo et al. 2011; Vautard et al. 2010). Equivalent studies over the ocean are lacking yet severely needed to better understand airflow and to constrain the momentum flux. This would be particularly helpful for tropical cyclone research where elevated roughness occurs over especially large spatial scales.

e. Cospectra

Characteristics of the flux are further revealed in the u–w cospectra (Fig. 9) for the beach tower (top) and pierhead (bottom). Each subplot shows the mean and 95% confidence

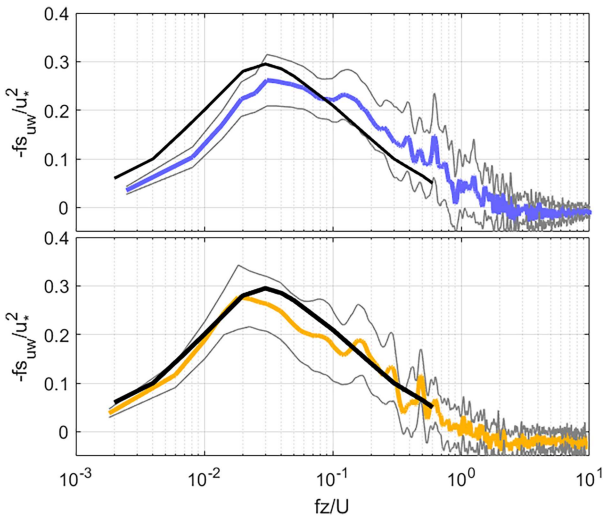

FIG. 9. Normalized mean u–w cospectra for data recorded on the (top) beach and (bottom) pierhead. Colored lines are means, gray lines are 95% confidence intervals, and the black curves are from Miyake et al. (1970).

interval from 0600 to 1200 local time 9 May (i.e., averaged over twelve 30-min runs) and plotted as a function of a dimensionless frequency. According to Monin–Obukhov similarity theory (Monin and Obukhov 1954), cospectra of wind velocity should follow a universal shape when scaled in this manner. Also shown is the universal curves of Miyake et al. (1970) , which comes from data collected over land and is generally used as the standard reference point for flux measurements (e.g., Ortiz-Suslow et al. 2020). In both cases, the cospectra assume a similar shape as Miyake et al. (1970) and those found elsewhere (e.g., Potter 2015, Lyu et al. 2021). However, for the surfzone measurement, the entire cospectrum is blue-shifted when compared with Miyake et al. (1970) and the pierhead. Consequently, there is much less energy at lower frequencies ($fz/U < 0.02$) and much more energy at higher frequencies ($fz/U < 0.01$), and the surfzone peak $fz/U = 0.031$ is also blue-shifted compared to $fz/U = 0.02$ at the pierhead.

Figure 9 indicates that the dominant eddies which transport energy in the surfzone at moderate to high winds have smaller wavelengths than elsewhere. In fact, they are more like TC turbulence than normal open ocean conditions. Zhang (2010) and Potter et al. (2015b) made direct flux measurements inside TCs and reported blue shifts in the u–w cospectra, like here. It is feasible that turbulence in TCs has similar properties to an energetic surfzone because both have steep and breaking waves, foam, and spray. Potter et al. (2015a) showed that the rapidly evolving, rotating wave field inside TCs creates *swell-like* conditions that have wind sea qualities because they were recently generated. However, due to the continuously shifting wind direction, these waves are no longer strictly wind sea. This so-called noncoherent wind sea is perhaps akin to waves in the surfzone which too have wind sea qualities (viz., high roughness) but are not wind driven. In both cases, the wind interacts with a very rough non–wind sea surface, which, to a greater or lesser extent, will alter the momentum exchange. Evidently, research opportunities exist to determine how processes nearshore can inform our understanding of TCs and vice versa. There is an entirely unique regime nearshore, especially in the surfzone, where open-ocean air–sea interaction norms do not necessarily apply. This is a major problem because it means we do not have the ability to predict the nearshore momentum flux or accurately model any nearshore wind-driven processes. More research studies in these areas are needed.

5. Summary and conclusions

In May 2022, a northeaster brought 20 m s^{-1} winds and 4-m significant wave heights to the Outer Banks of North Carolina. At that time, we were participating in an experiment at the Army Field Research Facility in Duck where sonic anemometers were mounted on a pierhead tower, ~500m offshore, and a beach tower slightly inland of the shoreline. During the storm, the drag coefficient observed at the pierhead was approximately equal to open-ocean values, but the drag coefficient measured at the beach was twice as large. Flux footprint analysis showed that the flux observed on the beach tower was sourced in the surfzone and the flux recorded at the pierhead was sourced well beyond the surfzone, meaning C_{Dz} at each location represented very different regimes. The surfzone drag coefficient increased quickly, which we attribute to the storm's rapid ramp which energized the surfzone increasing its coarseness. The surfzone flux was characterized by high-frequency-dominant turbulent transport, only previously observed in TCs. TCs have similar ocean surface properties as surfzones, but it remains unknown why the eddies in these unique environments are shorter than elsewhere. We hypothesize this occurs when the wind outpaces and interacts with an ocean surface that has strongly forced properties but is not windcoherent. Finally, we show that the wind speed decreased as it crossed the surfzone. We suggest that this occurred because the very rough surface dragged the wind slowing it. The precise mechanisms are unknown and further research is needed.

Acknowledgments. Funds provided by NSF Award 2319548 with support from Texas A&M and DUNEX. Thanks to FRF operations staff who provided invaluable support during the fieldwork and for many months after.

Data availability statement. The IRGASON and Gill sonic wind data used to determine the momentum flux in this study are available via the Texas Data Repository (https://doi.org/10.18738/T8/TXZKTM). All other data are available through the Field Research Facility data portal (https://frfdataportal.erdc.dren.mil/).

REFERENCES

Anguelova, M. D., and F. Webster, 2006: Whitecap coverage from satellite measurements: A first step toward modeling the

variability of oceanic whitecaps. *J. Geophys. Res.*, **111**, C03017, https://doi.org/10.1029/2005JC003158.

Ardhuin, F., T. H. C. Herbers, K. P. Watts, G. P. van Vledder, R. Jensen, and H. C. Graber, 2007: Swell and slanting-fetch effects on wind wave growth. *J. Phys. Oceanogr.*, **37**, 908–931, https://doi.org/10.1175/JPO3039.1.

Battjes, J. A., 1974: Surf similarity. *Coastal Engineering 1974*, American Society of Civil Engineers, 466–480, https://doi.org/10.1061/9780872621138.029.

Brodie, K., I. Conery, N. Cohn, N. Spore, and M. Palmsten, 2019: Spatial variability of coastal foredune evolution, part A: Timescales of months to years. *J. Mar. Sci. Eng.*, **7**, 124, https://doi.org/10.3390/jmse7050124.

Cialone, M. A., and Coauthors, 2023: A large-scale community storm processes field experiment: The During Nearshore Event Experiment (DUNEX) overview reference report. RDC/CHL TR-23-3, 158 pp.

Collins, C. O., III, H. Potter, B. Lund, H. Tamura, and H. C. Graber, 2018: Directional wave spectra observed during intense tropical cyclones. *J. Geophys. Res. Oceans*, **123**, 773–793, https://doi.org/10.1002/2017JC012943.

Constantin, A., 2021: Frictional effects in wind-driven ocean currents. *Geophys. Astrophys. Fluid Dyn.*, **115**, 1–14, https://doi.org/10.1080/03091929.2020.1748614.

Drennan, W. M., H. C. Graber, D. Hauser, and C. Quentin, 2003: On the wave age dependence of wind stress over pure wind seas. *J. Geophys. Res.*, **108**, 8062, https://doi.org/10.1029/2000JC000715.

Edson, J. B., and Coauthors, 2013: On the exchange of momentum over the open ocean. *J. Phys. Oceanogr.*, **43**, 1589–1610, https://doi.org/10.1175/JPO-D-12-0173.1.

French, J. R., W. M. Drennan, J. A. Zhang, and P. G. Black, 2007: Turbulent fluxes in the hurricane boundary layer. Part I: Momentum flux. *J. Atmos. Sci.*, **64**, 1089–1102, https://doi.org/10.1175/JAS3887.1.

Grachev, A. A., L. S. Leo, H. J. S. Fernando, C. W. Fairall, E. Creegan, B. W. Blomquist, A. J. Christman, and C. M. Hocut, 2018: Air–sea/land interaction in the coastal zone. *Bound.-Layer Meteor.*, **167**, 181–210, https://doi.org/10.1007/s10546-017-0326-2.

Guo, H., M. Xu, and Q. Hu, 2011: Changes in near-surface wind speed in China: 1969–2005. *Int. J. Climatol.*, **31**, 349–358, https://doi.org/10.1002/joc.2091.

Hansen, A., and J. MacMahan, 2019: Geometric roughness estimates of surf-zone wave-breaking foam. *Bound.-Layer Meteor.*, **170**, 183–190, https://doi.org/10.1007/s10546-018-0390-2.

Holman, R. A., and J. Stanley, 2007: The history and technical capabilities of Argus. *Coastal Eng.*, **54**, 477–491, https://doi.org/10.1016/j.coastaleng.2007.01.003.

Johnson, H. K., J. Højstrup, H. J. Vested, and S. E. Larsen, 1998: On the dependence of sea surface roughness on wind waves. *J. Phys. Oceanogr.*, **28**, 1702–1716, https://doi.org/10.1175/1520-0485(1998)028<1702:OTDOSS>2.0.CO;2.

Kljun, N., M. W. Rotach, and H. P. Schmid, 2002: A three-dimensional backward Lagrangian footprint model for a wide range of boundary-layer stratifications. *Bound.-Layer Meteor.*, **103**, 205–226, https://doi.org/10.1023/A:1014556300021.

——, P. Calanca, M. W. Rotach, and H. P. Schmid, 2015: A simple two-dimensional parameterisation for Flux Footprint Prediction (FFP). *Geosci. Model Dev.*, **8**, 3695–3713, https://doi.org/10.1023/A:1014556300021.

Lavers, D. A., A. Beljaars, D. S. Richardson, M. J. Rodwell, and F. Pappenberger, 2019: A forecast evaluation of planetary boundary layer height over the ocean. *J. Geophys. Res. Atmos.*, **124**, 4975–4984, https://doi.org/10.1029/2019JD030454.

Lee, J. H., and J. P. Monty, 2020: On the interaction between wind stress and waves: Wave growth and statistical properties of large waves. *J. Phys. Oceanogr.*, **50**, 383–397, https://doi.org/10.1175/JPO-D-19-0112.1.

Long, C. E., and J. M. Oltman-Shay, 1991: Directional characteristics of waves in shallow water. Coastal Engineering Research Center Tech. Rep. 91-1, 154 pp., https://apps.dtic.mil/sti/tr/pdf/ADA234568.pdf.

Lyu, M., H. Potter, and C. O. Collins, 2021: The impacts of gustiness on air–sea momentum flux. *Fluids*, **6**, 336, https://doi.org/10.3390/fluids6100336.

MacMahan, J., 2017: Increased aerodynamic roughness owing to surfzone foam. *J. Phys. Oceanogr.*, **47**, 2115–2122, https://doi.org/10.1175/JPO-D-17-0054.1.

Maddux, T. B., E. A. Cowen, D. L. Foster, M. C. Haller, and T. P. Stanton, 2007: The Cross-shore Sediment Transport Experiment (CROSSTEX). *Coastal Eng.*, **5**, 2547–2559, https://doi.org/10.1142/9789812709554_0215.

Mahrt, L., D. Vickers, J. Howell, J. Højstrup, J. M. Wilczak, J. Edson, and J. Hare, 1996: Sea surface drag coefficients in the Risø Air Sea Experiment. *J. Geophys. Res.*, **101**, 14 327–14 335, https://doi.org/10.1029/96JC00748.

Makin, V. K., 2005: A note on the drag of the sea surface at hurricane winds. *Bound.-Layer Meteor.*, **115**, 169–176, https://doi.org/10.1007/s10546-004-3647-x.

Manzella, E., T. Hara, and P. P. Sullivan, 2024: Reduction of drag coefficient due to misaligned wind-waves. *J. Geophys. Res. Oceans*, **129**, e2023JC020593, https://doi.org/10.1029/2023JC020593.

McMonigal, K., S. Larson, S. Hu, and R. Kramer, 2023: Historical changes in wind-driven ocean circulation can accelerate global warming. *Geophys. Res. Lett.*, **50**, e2023GL102846, https://doi.org/10.1029/2023GL102846.

Miyake, M., R. W. Stewart, and R. W. Burling, 1970: Spectra and cospectra of turbulence over water. *Quarterly Journal of the Royal Meteorological Society*, **96**, 138–143, https://doi.org/10.1002/qj.49709640714.

Monin, A. S., and A. M. Obukhov, 1954: Basic laws of turbulent mixing in the surface layer of the atmosphere. *Contrib. Geophys. Inst. Acad. Sci. USSR*, **151**, e163.

Obukhov, A. M., 1946: Turbulentnost'v temperaturnojneodnorodnoj atmosfere (turbulence in an atmosphere with a non-uniform temperature). *Tr. Inst. Theor. Geofiz.*, **792**, 95–115.

Oost, W. A., G. J. Komen, C. M. J. Jacobs, and C. Van Oort, 2002: New evidence for a relation between wind stress and wave age from measurements during ASGAMAGE. *Bound.-Layer Meteor.*, **103**, 409–438, https://doi.org/10.1023/A:1014913624535.

Ortiz-Suslow, D. G., B. K. Haus, N. J. Williams, N. J. M. Laxague, A. J. H. M. Reniers, and H. C. Graber, 2015: The spatial-temporal variability of air-sea momentum fluxes observed at a tidal inlet. *J. Geophys. Res. Oceans*, **120**, 660–676, https://doi.org/10.1002/2014JC010412.

——, ——, ——, H. C. Graber, and J. H. MacMahan, 2018: Observations of air-sea momentum flux variability across the inner shelf. *J. Geophys. Res. Oceans*, **123**, 8970–8993, https://doi.org/10.1029/2018JC014348.

——, Q. Wang, J. Kalogiros, and R. Yamaguchi, 2020: A method for identifying Kolmogorov's inertial subrange in the velocity variance spectrum. *J. Atmos. Oceanic Technol.*, **37**, 85–102, https://doi.org/10.1175/JTECH-D-19-0028.1.

——, J. Kalogiros, R. Yamaguchi, and Q. Wang, 2021: An evaluation of the constant flux layer in the atmospheric flow

above the wavy air-sea interface. *J. Geophys. Res. Atmos.*, **126**, e2020JD032834, https://doi.org/10.1029/2020JD032834.

Plant, N. G., and R. A. Holman, 1997: Intertidal beach profile estimation using video images. *Mar. Geol.*, **140**, 1–24, https://doi.org/10.1016/S0025-3227(97)00019-4.

Potter, H., 2015: Swell and the drag coefficient. *Ocean Dyn.*, **65**, 375–384, https://doi.org/10.1007/s10236-015-0811-4.

——, and J. E. Rudzin, 2021: Upper-ocean temperature variability in the Gulf of Mexico with implications for hurricane intensity. *J. Phys. Oceanogr.*, **51**, 3149–3162, https://doi.org/10.1175/JPO-D-21-0057.1.

——, C. O. Collins III, W. M. Drennan, and H. C. Graber, 2015a: Observations of wind stress direction during Typhoon Chaba (2010). *Geophys. Res. Lett.*, **42**, 9898–9905, https://doi.org/10.1002/2015GL065173.

——, H. C. Graber, N. J. Williams, C. O. Collins III, R. J. Ramos, and W. M. Drennan, 2015b: In situ measurements of momentum fluxes in typhoons. *J. Atmos. Sci.*, **72**, 104–118, https://doi.org/10.1175/JAS-D-14-0025.1.

——, C. O. Collins, and D. G. Ortiz-Suslow, 2022: Pier-based measurements of air-sea momentum fluxes over shoaling waves during DUNEX. *J. Geophys. Res. Oceans*, **127**, e2022JC018801, https://doi.org/10.1029/2022JC018801.

Pryor, S. C., and Coauthors, 2009: Wind speed trends over the contiguous United States. *J. Geophys. Res.*, **114**, D14105, https://doi.org/10.1029/2008JD011416.

Reniers, A. J. H. M., E. B. Thornton, T. P. Stanton, and J. A. Roelvink, 2004: Vertical flow structure during Sandy Duck: Observations and modeling. *Coastal Eng.*, **51**, 237–260, https://doi.org/10.1016/j.coastaleng.2004.02.001.

Reul, N., H. Branger, and J.-P. Giovanangeli, 1999: Air flow separation over unsteady breaking waves. *Phys. Fluids*, **11**, 1959–1961, https://doi.org/10.1063/1.870058.

Rey-Sanchez, C., A. Arias-Ortiz, K. Kasak, H. Chu, D. Szutu, J. Verfaillie, and D. Baldocchi, 2022: Detecting hot spots of methane flux using footprint-weighted flux maps. *J. Geophys. Res. Biogeosci.*, **127**, e2022JG006977, https://doi.org/10.1029/2022JG006977.

Sahlée, E., W. M. Drennan, H. Potter, and M. A. Rebozo, 2012: Waves and air-sea fluxes from a drifting ASIS buoy during the Southern Ocean Gas Exchange experiment. *J. Geophys. Res.*, **117**, C08003, https://doi.org/10.1029/2012JC008032.

Shabani, B., P. Nielsen, and T. Baldock, 2014: Direct measurements of wind stress over the surf zone. *J. Geophys. Res. Oceans*, **119**, 2949–2973, https://doi.org/10.1002/2013JC009585.

——, A. V. Babanin, and T. E. Baldock, 2016: Observations of the directional distribution of the wind energy input function over swell waves. *J. Geophys. Res. Oceans*, **121**, 1174–1193, https://doi.org/10.1002/2015JC011225.

Smith, S. D., 1980: Wind stress and heat flux over the ocean in gale force winds. *J. Phys. Oceanogr.*, **10**, 709–726, https://doi.org/10.1175/1520-0485(1980)010<0709:WSAHFO>2.0.CO;2.

——, and E. G. Banke, 1975: Variation of the sea surface drag coefficient with wind speed. *Quart. J. Roy. Meteor. Soc.*, **101**, 665–673, https://doi.org/10.1002/qj.49710142920.

Stockdon, H. F., R. A. Holman, P. A. Howd, and A. H. Sallenger Jr., 2006: Empirical parameterization of setup, swash, and runup. *Coastal Eng.*, **53**, 573–588, https://doi.org/10.1016/j.coastaleng.2005.12.005.

Vautard, R., J. Cattiaux, P. Yiou, J. N. Thépaut, and P. Ciais, 2010: Northern Hemisphere atmospheric stilling partly attributed to an increase in surface roughness. *Nat. Geosci.*, **3**, 756–761, https://doi.org/10.1038/ngeo979.

Vickers, D., and L. Mahrt, 2010: Sea-surface roughness lengths in the midlatitude coastal zone. *Quart. J. Roy. Meteor. Soc.*, **136**, 1089–1093, https://doi.org/10.1002/qj.617.

Vugts, H. F., and F. Cannemeijer, 1981: Measurements of drag coefficients and roughness length at a sea-beach interface. *J. Appl. Meteor.*, **20**, 335–340, https://doi.org/10.1175/1520-0450(1981)020<0335:MODCAR>2.0.CO;2.

Wang, Q., and Coauthors,2018: CASPER: Coupled Air–Sea Processes and Electromagnetic ducting Research. *Bull. Amer. Meteor. Soc.*, **99**, 1449–1471, https://doi.org/10.1175/BAMS-D-16-0046.1.

Wu, L., and F. Qiao, 2022: Wind profile in the wave boundary layer and its application in a coupled atmosphere-wave model. *J. Geophys. Res. Oceans*, **127**, e2021JC018123, https://doi.org/10.1029/2021JC018123.

Yelland, M., and P. K. Taylor, 1996: Wind stress measurements from the open ocean. *J. Phys. Oceanogr.*, **26**, 541–558, https://doi.org/10.1175/1520-0485(1996)026<0541:WSMFTO>2.0.CO;2.

Zhang, F. W., W. M. Drennan, B. K. Haus, and H. C. Graber, 2009: On wind-wave-current interactions during the Shoaling Waves Experiment. *J. Geophys. Res.*, **114**, C01018, https://doi.org/10.1029/2008JC004998.

Zhang, J. A., 2010: Spectral characteristics of turbulence in the hurricane boundary layer over the ocean between the outer rain bands. *Quart. J. Roy. Meteor. Soc.*, **136**, 918–926, https://doi.org/10.1002/qj.610.